Research Square

Preprints are preliminary reports that have not undergone peer review.
They should not be considered conclusive, used to inform clinical practice,
or referenced by the media as validated information.

Non-Volatile Tunable Chiroptical Responses of GSST-Ge Hybrid Quasi-BIC Active Metasurfaces in the Mid-Infrared Regime

Zhijin Huang

zhijinhuang2022@gdmec.edu.cn

Guangdong Mechanical and Electrical Polytechnic

Junzhong Wang

Guangdong Mechanical and Electrical Polytechnic

Juan Wang

Guangdong Mechanical and Electrical Polytechnic

Research Article

Keywords: Active metasurface, Bound states in the continuum, Circular polarization manipulation, Phase-change material, Ge2Sb2Se4Te (GSST)

Posted Date: November 17th, 2026

DOI: https://doi.org/10.21203/rs.3.rs-11498824/v1

License: This work is licensed under a Creative Commons Attribution 4.0 International License.
Read Full License

Additional Declarations: No competing interests reported.

Non-Volatile Tunable Chiroptical Responses of GSST-Ge Hybrid Quasi-BIC Active Metasurfaces in the Mid-Infrared Regime

Zhijin Huang*, Junzhong Wang, Juan Wang

School of Electronic Information, Guangdong Mechanical and Electrical Polytechnic, Guangzhou 510500, China.

**Corresponding author*: zhijinhuang2022@gdmec.edu.cn

Abstract

Dynamic polarization state manipulation at the nanoscale is highly desirable for emerging photonic applications. Here, we theoretically demonstrate a reconfigurable chiral metasurface based on quasi-bound states in the continuum (*quasi*-BIC) and the chalcogenide phase-change material $Ge_2Sb_2Se_4Te$ (GSST). By combining Ge and GSST elliptical dimers, the proposed structure achieves a *quasi*-BIC resonance with $Q\approx8390$ dominated by magnetic dipole resonances, ensuring strong near-field enhancement. Benefiting from the substantial and near-lossless refractive index contrast of GSST ($\Delta n\approx1.5$), the metasurface delivers a dramatic circular dichroism (CD) modulation ranging from -0.3 to -1 across the 6∼8 μm mid-infrared band. Crucially, the phase change induces a large resonance wavelength shift of $\Delta\lambda$=1.2 μm, which drives a continuous polarization evolution across the Poincaré sphere. By dynamically tuning the crystallization ratio (C from 0 to 1), we achieve continuous polarization conversion from elliptical toward near-circular polarization states. This high-performance platform provides a promising paradigm for active infrared meta-optics, including tunable lenses, dynamic holography, and polarization-encoded computing.

Keywords: Active metasurface; Bound states in the continuum; Circular polarization manipulation; Phase-change material; $Ge_2Sb_2Se_4Te$ (GSST)

1. Introduction

Dynamic polarization control represents a fundamental challenge in contemporary nanophotonics, with important applications including quantum information processing(Crotti et al. 2024), holographic displays(Xiong et al. 2023), dynamic chiral sensing(Wang et al. 2026), and optical communication(Chen et al. 2025a). Conventionally, polarization manipulation relies on bulk materials such as liquid crystals(Pitilakis et al. 2022), plasmonic helical nanoantennas(Wang et al. 2021), and supramolecular chiral materials(Li et al. 2025). Such devices typically demand elaborate spatial architectures and suffer from low modulation efficiency. Chiral plasmonic micro/nanostructures (e.g., gammadions and Z-shaped antennas) provide strong chiral responses, yet they cannot simultaneously sustain high-quality resonances and high modulation efficiency due to intrinsic ohmic losses(He et al. 2022; Zeng et al. 2023).

Recently, bound states in the continuum (BICs) have emerged as a promising route to address this limitation(He et al. 2018; Hsu et al. 2016; Kang et al. 2023; Koshelev et al. 2019). BICs lie inside the radiation continuum while possessing an ideal infinite quality factor (Q-factor) and appear dark for normally incident plane waves. Introducing controlled geometric perturbations to convert a BIC into a quasi-BIC creates an attractive platform for realizing high-Q resonances and tailored polarized emission. For instance, Liu et al. demonstrated circularly polarized states by breaking the in-plane inversion symmetry of a two-dimensional photonic-crystal slab(Liu et al. 2019). Overvig et al. theoretically verified that symmetry-protected BICs can expand the accessible polarization-state space(Overvig et al. 2021). In 2023, Chen et al. reported intrinsic chiral BICs exhibiting giant circular dichroism (CD) via weak tilt perturbations(Chen et al. 2023). These advances have greatly enriched chiral light–matter interactions; nevertheless, flexible polarization reconfiguration enabled by quasi-BIC resonances remains highly desirable(Guan et al. 2025; Xie et al. 2024; Yang et al. 2025).

Active metasurfaces, which merge conventional metasurface geometries with dynamically tunable functional materials(Chen et al. 2025b; Crotti et al. 2024; Cui et al. 2019), have achieved substantial progress in modulating optical amplitude, frequency, and polarization(Pitilakis et al. 2022). However, metasurfaces integrated with semiconductors (Si, GaAs, conductive oxides) or two-dimensional materials (graphene, perovskites) suffer from considerable parasitic absorption originating from free-carrier effects(Kim and Cho 2024; Ma et al. 2023). Phase-change materials (PCMs) are appealing owing to their large refractive-index contrast. Among them, VO_2 exhibits a volatile insulator–metal transition and requires a steady thermal bias to retain its metallic phase(Jiang et al. 2024; Mahmud et al. 2024; P et al. 2020), whereas the GST family delivers prominent non-volatile index contrast at the cost of relatively high optical absorption(Ding et al. 2021; Jiang et al. 2023a; Ouyang et al. 2024). It is therefore imperative to identify PCMs whose structural phase transition enables refractive-index modulation with suppressed excess loss for flexible quasi-BIC-based polarization control(Jiang et al. 2023b; Wang et al. 2024).

Within the family of PCMs, GSST has attracted intensive attention thanks to its broadband infrared transparency spanning 1–18.5 μm and an exceptionally high figure of merit (FOM) in the mid-infrared(Aryana et al. 2021; Svoboda et al. 2015; Tang et al. 2025). GSST offers a large refractive-index contrast ($\Delta n \approx 1.5$) across its amorphous-to-crystalline transformation, accompanied by markedly lower absorption compared with conventional GST(Zhang et al. 2021; Zhang et al. 2019). Recent works have demonstrated GSST-based chiral metasurfaces for tunable CD and reversible chiral transmission(Hu et al. 2023; Shi et al. 2023; Wu et al. 2024), as well as GSST-integrated quasi-BIC systems for ultra-high-Q dynamical modulation(Cheng et al. 2024; Zhou et al. 2023).Prior investigations have demonstrated GSST-integrated quasi-BIC metasurfaces for *Q*-factor modulation and GSST chiral metasurfaces for discrete circular dichroism switching. Nevertheless, constructing GSST-based hybrid active metasurfaces empowered by chiral quasi-BIC to achieve non-volatile continuous evolution of chiroptical responses and polarization states in the mid-infrared regime still remains largely unexplored.

In this work, we theoretically propose a mid-infrared phase-change-active metasurface for flexible polarization manipulation using GSST. The hybrid metasurface consists of elliptical Ge and GSST subwavelength resonators. A giant CD of the quasi-BIC is obtained by simultaneously breaking the in-plane inversion symmetry and out-of-plane mirror symmetry via judiciously engineered rotation and tilt angles. Multipole decomposition confirms that this quasi-BIC is dominated by magnetic-dipole (MD) contributions, yielding a high simulated Q-factor of 8390 under ideal lossless geometric conditions. After geometric optimization, we obtain a large CD up to 0.998 within the 6–8 μm spectral band. Our platform provides a viable route toward mid-infrared active nanophotonic devices for vector holography, optical computing, and polarization sensing.

2. Structure Design and Quasi-BIC Mechanism

2.1 Structural Configuration

As illustrated in Fig.1(a), the schematic diagram of the proposed hybrid metasurface, consisting of Ge and GSST elliptical resonators deposited on SiO_2 substrate. The reason for choosing Ge and GSST to construct the hybrid metasurface is that Ge has a large permittivity constant (ε_{Ge}~11.7) compared with GSST (ε_{GSST}~11.7) and low optical losses in the infrared regime. The metasurface has a planar lattice with the same periodicity (as shown in Fig.1(b)) along both *x* and *y* directions P*x*=P*y*=3.5μm. The initial position of resonator is expressed as (x_0, y_0), where x_0=0.7μm and y_0=0.25μm, leaving sufficient space for the modification of geometric parameters. The Ge and GSST resonators in single unit cell possess the same lengths Ly_1=Ly_2=2.2μm and slab thickness H=1μm, but different with of W$_{x1}$ and W$_{x2}$.

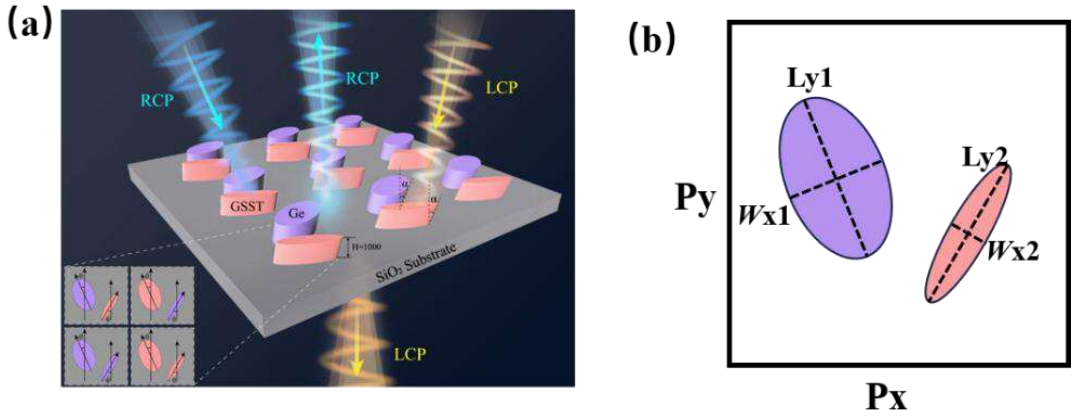


Fig.1 (a)Schematic diagram of the proposed active optical quasi-BIC metasurface. The inset shows xy-plane of the unit cell of the metasurface formed by the Ge-GSST submicron resonators. (b) the top view of the metasurface. The geometrical parameters P_x=P_y=3.5μm, L_{y1}=L_{y2}=2.2μm, W_{x1}=0.75μm, W_{x2}=0.25μm.

To construct chiral hybrid metasurfaces, we introduce width difference asymmetry parameter δ to break in plane mirror symmetry of the unit cell, defined as

$$\delta = \frac{(W_{x1} - W_{x2})}{(W_{x1} + W_{x2})} \tag{1}$$

Non-zero δ introduces in-plane geometric asymmetry. In our design strategy, we reduce the width of one elliptical resonator while enlarging the counterpart, as sketched within Fig.1(b) inset. To suppress symmetry perturbation from the substrate, the whole metasurface is embedded in homogeneous background medium with refractive index (n=1.45), approximately preserving out-of-plane mirror symmetry. Optical constants for GSST and Ge are extracted from published literature(Svoboda et al. 2015) and Palik Handbook(Icenogle et al. 1976), respectively.

2.2 Quasi-BIC Mechanism

To uncover the underlying physical principles of Ge-GSST hybrid metasurface, we analyze the bandstructures by implementing Electromagnetic Wave Frequency Domain module of COMSOL Multiphysics based on the finite element method. In the full-wave simulation, perfect matching layer (PML) conditions are applied at the upper and lower boundaries along the z-direction while periodic boundary conditions are imposed in the transverse directions to replicate an infinite array(Xu et al. 2026; Ye et al. 2024; Zeng et al. 2025; Zhang et al. 2024). It should be noted that this setup is dedicated to band-structure eigenmode analysis in this section and Section 3. In Section 4 and Section 5, the refractive indices of GSST will be modified according to amorphous/crystalline phases for phase-change dynamic transmission simulations.

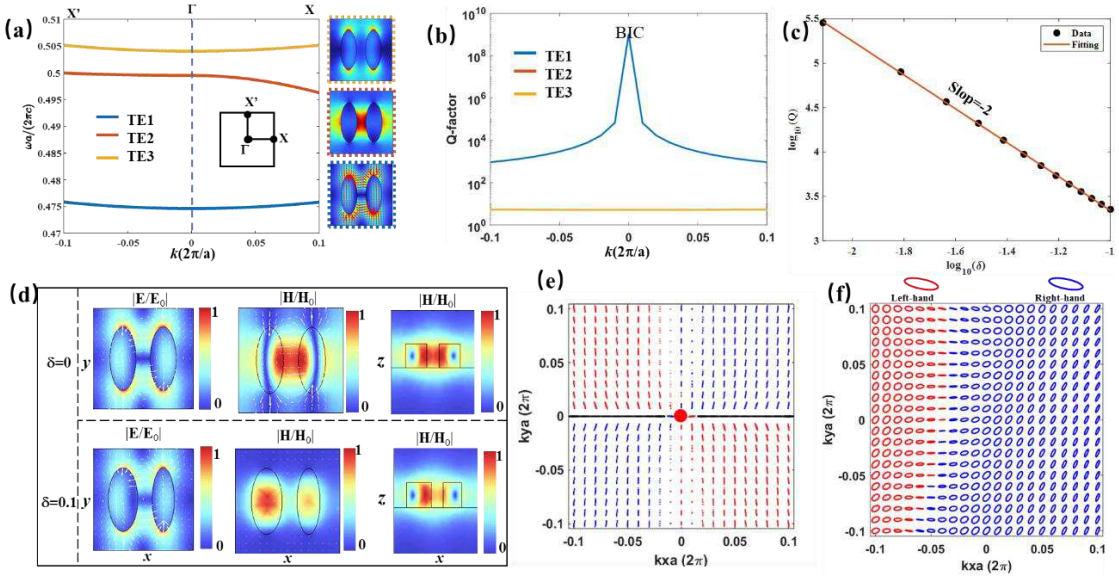


Fig.2 (a) Band structure along X′→Γ→X (k from -0.1 to 0.1), with TE_1, TE_2, and TE_3 modes at normalized frequencies of 0.475, 0.500, and 0.505. Insets: magnetic field distributions (0-1) and the first Brillouin zone. (b) Q-factors in k-space. The TE_1 mode exhibits a symmetry-protected BIC at the Γ point with Q spiking to ~10^9, while TE_2/TE_3 are low-Q modes. (c) Log-log plot of Q-factor vs. asymmetry δ. The fitting exhibits a slope of -2 for δ ranging from 10^{-2} to 10^{-1} (Q drops from ~10^5 to ~10^3). (d) Near-field distributions ($|E/E_0|$) and ($|H/H_0|$) at δ=0 and δ=0.1. (e-f) Momentum-space polarization states (e) for δ=0 and (f) for δ=0.1. The red point represents the singularity of polarization. The broken symmetry induces left-hand (red circles) and right-hand (blue ellipses) elliptical polarizations.

The band structure and Q-factors were mapped along the X′→Γ→X direction of the first Brillouin zone. As shown in Fig.2(a), exactly three transverse electric (TE) modes emerge near the Γ point. Within the normalized frequency range of $\omega a/2\pi c$ =0.47 to 0.51, the TE_1, TE_2, and TE_3 modes are located at approximate normalized frequencies of 0.475, 0.500, and 0.505, respectively. The TE_1 mode exhibits an infinite Q-factor at the Γ point (k_x=0), identifying it as a symmetry-protected BIC (SP-BIC). Numerically, as shown in Fig.2(b) (plotted from k_x =−0.1 to 0.10.1), the Q-factor is extracted via Q=Re(ω)/(2Im(ω)), where Re(ω) and Im(ω) are the real and imaginary parts of the complex eigenfrequency(Hu et al. 2022; Lai et al. 2025; Zeng et al. 2024) . Crucially, the Q-factor of TE_1 at the BIC point spikes to approximately 10^9, while TE_2 and TE_3 remain at a low-Q modes. When introducing an in-plane width asymmetry δ, the quality factor follows $Q \propto \delta^{-2}$ (in Fig. 2(c)), which is a typical signature of an SP-BIC(Chen et al. 2026; Hu et al. 2024; Liu et al. 2019). The numerical fitting in Fig.2(c) shows a slope of exactly -2 in the log10(Q) versus log10(δ) plot, with δ ranging from 10^{-2} to 10^{-1} and Q ranging from 2.5×10^3 to 3×10^5. As illustrated in Fig. 2(d), the field distributions change from a highly symmetric profile at δ=0 to an asymmetric one at δ=0.1.

Furthermore, the momentum-space polarization states are depicted in Fig.2(e) and 2(f), where the ideal BIC exhibits purely linear polarization(Kang et al. 2022; Liu et al. 2019), and the non-zero asymmetry δ induces the emergence of left-hand (red circles) and right-hand (blue ellipses) elliptical polarizations, confirming that introducing a non-zero δ directly breaks the in-plane symmetry and triggers the change from an ideal BIC to a leaky quasi-BIC.

3. Results and Discussion

3.1 Geometric Optimization for Chiral Quasi-BIC

To elucidate the underlying physical mechanism and maximize the chiroptical response, we

investigated the geometric parameter dependence of the quasi-BIC resonance (Fig.3). As illustrated in Fig.3(a), the structural geometry is tailored by two distinct parameters: an in-plane rotation angle θ and an out-of-plane tilt angle α. As shown in Fig.3(b), increasing the in-plane rotation θ induces a continuous wavelength blueshift. Specifically, at α=5°, the resonance wavelength decreases from 7.189 μm to 7.184 μm as θ increases to10°. Notably, increasing the tilt angle α causes an overall redshift of the resonance, reflecting the changed effective refractive index of the environment.

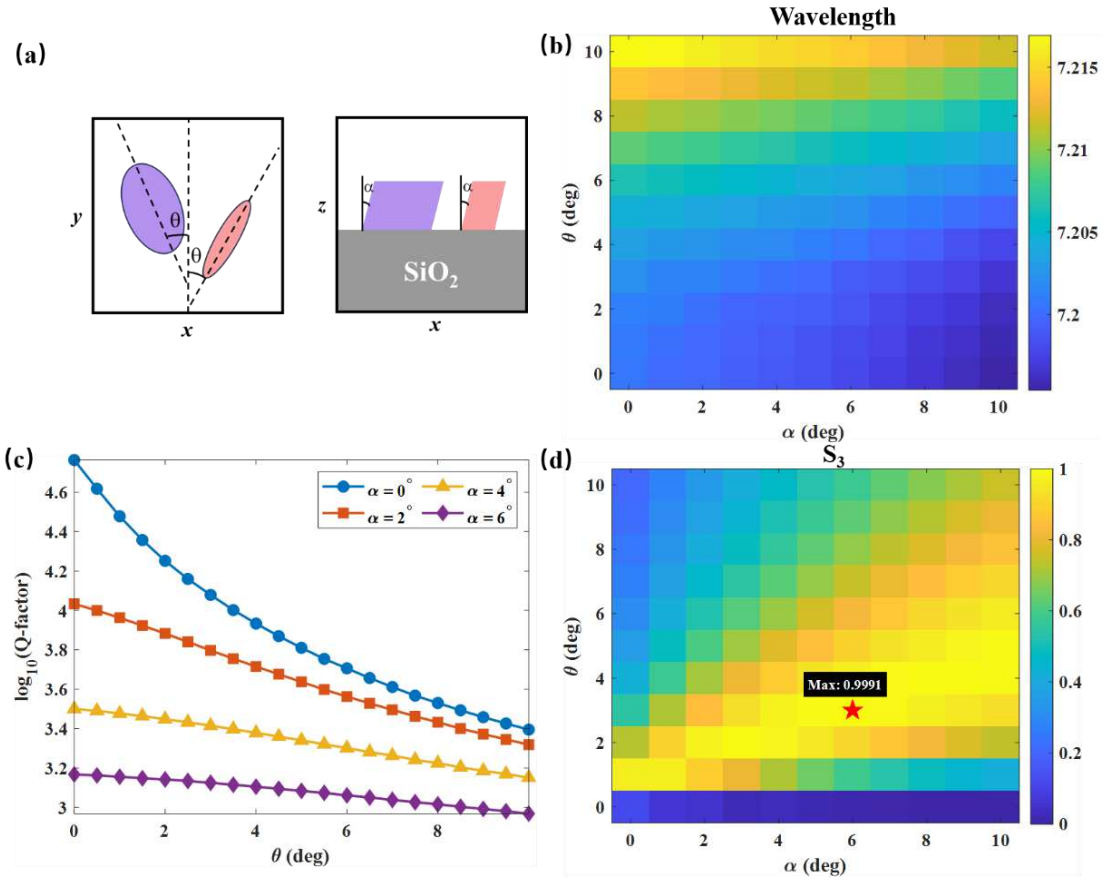


Fig. 3. Geometric parameter optimization for the quasi-BIC resonance. (a) Schematic of a single cell. The elliptical submicron-resonators are tailored by an in-plane rotation angle θ and an out-of-plane tilt angle α.(b) Eigen-wavelength of the resonance, showing a continuous blueshift with increasing θ (e.g., from 7.189 to 7.184 μm for α=5°) and an overall redshift with increasing α. (c)Semi-logarithmic plot of quality factors versus rotation angle θ. The Q-factor monotonically decreases with increasing θ due to the opening of radiation channels. For α=0°, it drops from 30038 to 2483.5 as θ increases from 2° to 10°. Introducing the out-of-plane tilt α further lowers the overall Q-factor due to additional out-of-plane radiation losses. (d) Stokes parameter S_3, demonstrating a significant chirality enhancement from a weak -0.2 (α=0°) to near-unity peaks of 0.93 (α=3°) and 0.97 (α=5°). The maximum S_3 of 0.9991 is achieved at α=6°,θ=3°.

To quantitatively validate the symmetry-protected nature of the quasi-BIC, we extracted the Q-factors under different perturbations, as shown in the semi-logarithmic plot in Fig.3(c). For the purely in-plane symmetry breaking case (α=0°), the Q-factor drops drastically as the rotation angle θ increases. For instance, it decreases from 30038 at θ=1° to 2483.5 at θ=10°, indicating that the in-plane rotation opens the primary radiation leakage channel. Furthermore, introducing an out-of-plane tilt (α>0°) fundamentally lowers the overall Q-factor because the tilt breaks the vertical mirror symmetry and introduces additional out-of-plane radiation channels. As a result, even at θ=0°, the Q-factor is reduced from 57938 (at α=0°) to 1471.5 (at α=6°), and it further drops to 929.97 at α=6°,θ=10°. This continuous

degradation of the Q-factor confirms that both in-plane and out-of-plane asymmetries synergistically contribute to the radiation losses of the quasi-BIC mode.

To evaluate the chiroptical response, the Stokes parameter S_3 was calculated (Fig. 3(d)). Purely in-plane symmetry breaking (α=0°) produces only a weak chirality, with S_3 remaining around -0.2. In sharp contrast, introducing the out-of-plane tilt fundamentally breaks the vertical mirror symmetry (z-direction) of the structure. This simultaneous breaking of both in-plane and out-of-plane symmetries drastically amplifies the chiral response. As a result, S_3 reaches peak values of 0.93 at α=3°,θ=6° and 0.97 at α=5°,θ=9°, achieving near-unity circular polarization conversion. The global maximum of S_3 reaches 0.9991 at α=6°,θ=3°, demonstrating a giant chirality driven by the synergistic symmetry-breaking effect.

3.2 Large Circular Dichroism Mechanism

To gain deeper insight into the optical chirality of the quasi-BIC, the circular dichroism (CD) is calculated based on the transmittance difference under RCP and LCP illuminations(Chen et al. 2023; Overvig et al. 2021; Yang et al. 2025) :

$$CD = \frac{(T_{rr} + T_{lr}) - (T_{rl} + T_{ll})}{(T_{rr} + T_{lr}) + (T_{rl} + T_{ll})} \tag{2}$$

Here, $T_{ij}=|t_{ij}|^2$ (r: RCP; l: LCP) is the transmittance of output polarization i from the input polarization j, and all element of t_{ij} construct the Jones matrix under circular polarization basic(Xia et al. 2026; Ye et al. 2024; Zhang et al. 2024) :

$$J_{circ} = \begin{pmatrix} t_{rr} & t_{rl} \\ t_{lr} & t_{ll} \end{pmatrix} \tag{3}$$

The results are shown in Fig.4(a), displaying the transmittances (T_{rr}, T_{rl}, T_{ll}, T_{lr}) and CD as functions of wavelength, with the inset showing the structural schematic of the rotated elliptical resonators. Near the quasi-BIC resonance at λ=7.2 μm, a drastic polarization conversion emerges: the cross-polarized transmittance T_{lr} (green dashed curve) approaches nearly 1, while T_{rl} (red dotted curve) exhibits a deep valley approaching 0. This extreme discrepancy drives the CD (purple solid curve) to a large value nearly 0.998. The Fano fitting for the RCP transmittance spectrum yields an evaluated Q-factor of 8390 (see Section S1 in the Supporting Information).

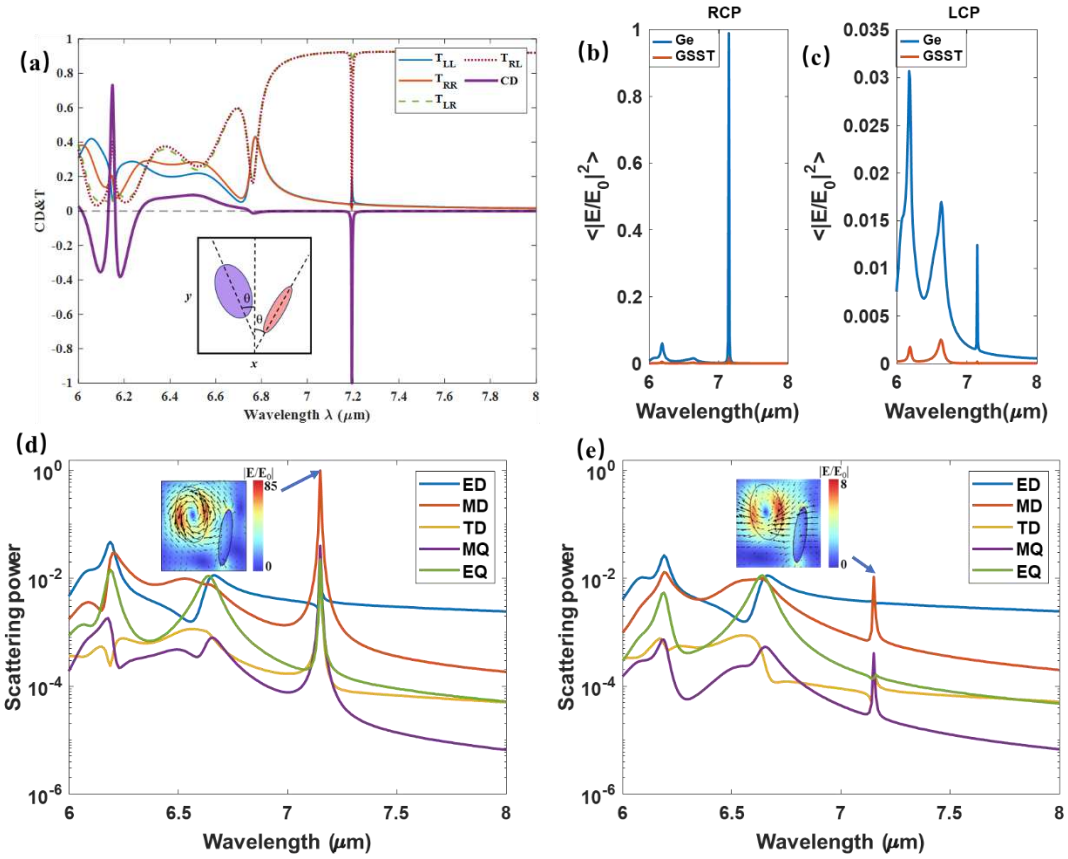


Fig.4. Optical chirality and multipolar analysis of the quasi-BIC metasurface. (a) Transmittances and CD under normal incidence. At λ=7.2μm, T_{RL}≈1 and T_{LR}≈0 yield a giant CD of 0.998. Inset: structural schematic and Fano fitting (Q=8390). (b-c) Averaged intensity enhancement (<$|E/E_0|^2$>) for Ge (blue) and GSST (orange) under (b) RCP and (c) LCP illuminations. The Averaged intensity enhancement of Ge reaches 1 at λ=7.2 μm under RCP, but is strongly suppressed under LCP. (d-e) Multipolar scattering power under (d) RCP and (e) LCP illuminations, dominated by MD at λ=7.2 μm. Insets: near-field distributions at λ=7.2μm.

To elucidate the physical origin of this large CD, Figs.4(b) and 4(c) depict the wavelength-dependent electric field intensities ($|E/E_0|^2$) for both Ge and GSST micro-resonators. Under RCP illumination (Fig.4(b)), the Ge resonator (blue curve) exhibits an intense field enhancement, reaching a maximum normalized intensity of 1 at 7.15 μm, whereas the GSST structure (orange curve) shows near-zero intensity. Conversely, under LCP illumination (Fig.4(c)), the field intensity for the Ge resonator at 7.15 μm is drastically suppressed to approximately 0.005 (peaking elsewhere at ~0.033). This pronounced discrepancy in field localization directly accounts for the drastic transmittance difference (T_{lr}≫T_{rl}) and fundamentally drives the ultrahigh CD of the quasi-BIC mode(Sharma et al. 2025; Xu et al. 2026) .

To further reveal the mode nature, we further perform multipole-decomposition analysis to reveal scattering characteristics under circularly-polarized incidence (see Section S2 in the Supporting Information). Around λ=7.15 μm, the far field scattering under RCP excitation mainly originates from the contributions of the magnetic dipole (MD) and electric dipole (ED). It should be emphasized that these multipole components represent the scattering response excited by external RCP illumination, rather than the intrinsic property of the quasi-BIC eigenmode. For LCP incidence, the aforementioned multipole scattering responses are substantially suppressed. The near-field insets exhibit typical spatial profiles of dipole resonance(Jia et al. 2025; Lee et al. 2023), which confirms that the selective excitation of MD-dominated scattering under RCP, combined with the strong suppression under LCP,

fundamentally drives the observed giant CD.

4. Dynamic Polarization Control via GSST Phase Change

4.1 Crystallization-Dependent Dielectric Tuning

The dielectric properties of GSST undergo a reversible change between its amorphous state (characterized by a lower permittivity ε_a=10.56) and crystalline state (higher permittivity ε_c=22.56) at the operational wavelength of 7.2μm(Svoboda et al. 2015) . To quantitatively describe the effective dielectric response at intermediate crystallization ratios C (0≤C≤1), We adopt the Lorentz-Lorenz effective-medium theory to approximate partially-crystallized GSST. We note that this EMT assumes spherical inclusions; real GSST partial crystallization forms polycrystalline thin films, which may introduce deviations in practical experiments. This model relates the effective permittivity $\varepsilon_{\mathrm{GSST}}^{\mathrm{eff}}$ to the crystallization ratio through the expression (Cheng et al. 2024; Tang et al. 2025) :

$$\frac{\varepsilon_{\mathrm{GSST}}^{\mathrm{eff}}-1}{\varepsilon_{\mathrm{GSST}}^{\mathrm{eff}}+2}=C\frac{\varepsilon_c-1}{\varepsilon_c+2}+(1-C)\frac{\varepsilon_a-1}{\varepsilon_a+2} \tag{4}$$

Continuous variation of C from 0 to 1 enables monotonic tuning of $\varepsilon_{\mathrm{GSST}}^{\mathrm{eff}}$ from ε_a and ε_c, corresponding to a refractive index shift of Δn≈1.5 while maintaining ultralow optical loss. Crucially, this near-lossless refractive index modulation directly perturbs the hybridized quasi-BIC resonance, inducing spectral shifts up to Δλ=1.2μm, which is leveraged in polarization state engineering. The accuracy of this EMT framework is validated by the nonlinear trajectory of trajectory of $\varepsilon_{\mathrm{GSST}}^{\mathrm{eff}}(C)$ shown in Fig.6c (inset), establishing a critical foundation for thermally driven dynamic control.

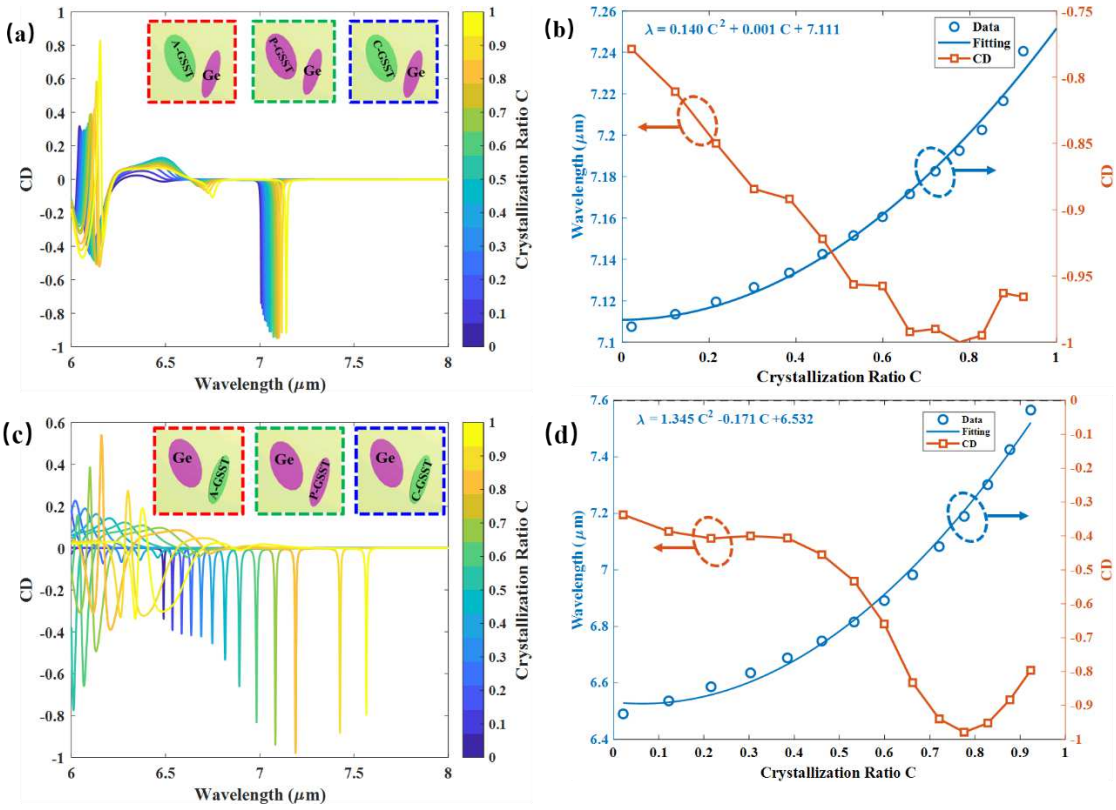


Fig.5. Configuration-dependent circular dichroism (CD) spectra and their evolution. (a) Calculated CD spectra for the Ge-GSST configuration (larger Ge and smaller GSST resonators, insets) at different crystallization ratios C (0 to 1). (b) Evolution of the resonant wavelength and maximum CD for the Ge-GSST configuration. As Cincreases, the wavelength redshifts from 7.111 μm to ~7.25 μm (fitted by a quadratic polynomial), and the CD reaches nearly -1. (c) Calculated CD spectra for the GSST-Ge configuration (larger GSST and smaller Ge resonators). (d) Evolution of the resonant wavelength and maximum CD for the GSST-

Ge configuration. The wavelength exhibits a redshift from ~6.53 μm to ~7.1 μm, with the CD reaching nearly -1.

To investigate the influence of different Ge-GSST configurations on circular dichroism (CD), we considered six distinct arrangements. The refractive index of the Ge resonator is fixed at 4.17 within the 6-8 range, while that of GSST varies from 3.25 to 4.57, corresponding to its phase change from the amorphous (A-GSST) to the crystalline (C-GSST) state. As depicted in Fig.5(a), when the Ge resonator is larger than the GSST resonator, the CD spectrum exhibits a blueshift as GSST changes from the A-state (red box) to the C-state (blue box). Specifically, the maximum CD wavelength shifts from approximately 7.15 μm to 7.25 μm, with the CD value remaining near -1. By continuously tuning the crystallization ratio C (Fig.5(b)), the resonant wavelength follows a quadratic relation: $\lambda=0.140C^2-0.001C+7.111$(in μm), confirming a continuous tuning capability.

Conversely, when the GSST resonator is larger than the Ge resonator (Fig.5(c)), the CD spectrum exhibits a pronounced redshift with increasing C, accompanied by a significant shift in the wavelength of the maximum CD. This phenomenon is attributed to the fact that light energy is highly confined within the larger resonator, where the electric field intensity contrast reaches up to two orders of magnitude. Consequently, the refractive index variation induces strong light-matter interactions. As summarized in Fig.5(d), the q-BIC wavelength undergoes a massive continuous redshift from 6.5 μm to 7.8μm ($\Delta\lambda$=1.3um). The nonlinear evolution is well-described by the fitted curve $\lambda=1.345C^2-0.171C+6.532$[μm]. This quadratic CD wavelength shift stems from the volume-dependent field-localization effect(Xu et al. 2026; Xu et al. 2024; Zeng et al. 2025), which explains the large index variation (Δn=1.5) dynamically alters the optical mode confinement in GSST resonator, collectively causing the CD wavelength to deviate from a simple linear dependence.

4.2 Evolution of Polarization States

To investigate the continuous polarization transformation on the Poincaré sphere driven by the controlled crystallization of the GSST resonator, the evolution from the amorphous (C=0) to the fully crystalline (C=1) state is mapped. As shown in Fig.6, the Stokes parameters evolve along a deterministic trajectory, originating from an elliptical polarization state and culminating in a near-circular state (see Section S3 in the Supporting Information). This trajectory reveals two synchronized phenomena: the progressive enhancement of ellipticity and the azimuthal rotation.

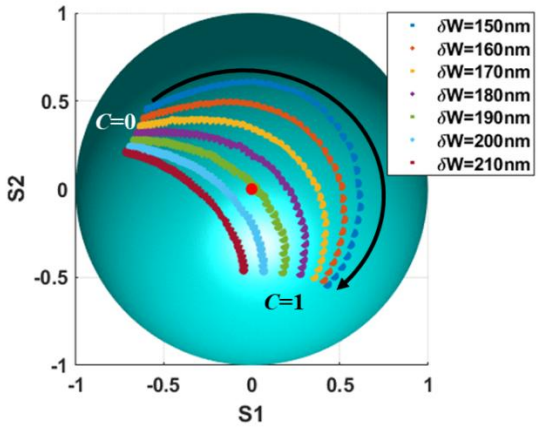


Fig.6 Stokes trajectory of the metasurfaces by controlling the crystallization ratio C of GSST resonator. The red dot marks an intermediate point on the polarization trajectory. The north pole (S_1, S_2, S_3) = (0,0,1) corresponds to ideal right-hand circular polarization

5. Conclusion

In summary, we numerically investigated dynamic mid-infrared(λ=6~8μm) polarization

manipulation based on a Ge-GSST hybrid active metasurface supporting magnetic-dipole-dominated symmetry-protected quasi-BIC. Introducing in-plane geometric asymmetry transforms ideal BIC into quasi-BIC with (Q~8390), yielding giant circular dichroism (CD≈1) via asymmetric multipole interference between RCP and LCP excitations. Leveraging the near-lossless refractive-index contrast (Δn≈1.5) of GSST, varying the crystallization ratio *C* from 0 to 1 produces a resonant wavelength redshift of ($\Delta\lambda$≈1.2 μm), enabling continuous polarization evolution from elliptical to near-circular states on the Poincaré sphere. This work validates phase-change-integrated high-Q quasi-BIC metasurfaces for reconfigurable polarization control, providing a feasible route toward tunable mid-infrared meta-devices for chiral sensing, dynamic holography and polarization-encoded computing.

Supporting Information

This document contains supplementary information organized as follows: S1. Detailed Fano fitting of the quasi-BIC resonances under LCP and RCP normal illumination to extract the Q-factor. S2. Theoretical formulations and scattering power decomposition to reveal the physical origin of the quasi-BIC resonance. S3. Calculation methodology of the Stokes parameter to evaluate the chiroptical response.

Author contributions

Zhijin Huang: Conceptualization, Methodology, Formal analysis, Investigation, Writing-original draft, Writing-review & editing, Supervision, Project administration, Funding acquisition; Junzhong Wang: Methodology, Formal analysis, Investigation, Visualization, Writing-review & editing; Juan Wang: Investigation, Visualization, Validation, Writing-review & editing.

Funding

We obtain the financial supports from the High-level Talents Project of Guangdong Mechanical & Electrical Polytechnic (Gccrcxm-202208); The Guangdong Provincial Ordinary University Characteristic Innovation Project (2023KQNCX164).

Data availability

The datasets generated during the current study are available from the corresponding author on reasonable request.

Declaration of competing interest

The authors declare no competing interests.

References

Aryana, K., Zhang, Y., Tomko, J.A., Hoque, M.S. Bin, Hoglund, E.R., Olson, D.H., Nag, J., Read, J.C., Ríos, C., Hu, J., Hopkins, P.E.: Suppressed electronic contribution in thermal conductivity of Ge2Sb2Se4Te. Nature Communications . 12, (2021). https://doi.org/10.1038/s41467-021-27121-x

Chen, C., Yang, Z., Hang, T., Hao, Y., Chen, Y., Zhang, C., Yang, J., Liu, X., Li, X., Cao, G.: Electrical-gain-assisted circularly polarized photodetection based on chiral plasmonic metamaterials. Light Sci. Appl. 14, (2025)(a). https://doi.org/10.1038/s41377-025-01932-9

Chen, H., Dai, P., Wang, W., Yin, R., Zeng, L., Du, J., Wang, W., Kuang, X.: High-CD chiral metasurfaces with robustness and active tunability via bound states in the continuum. Opt. Commun. 595, (2025)(b). https://doi.org/10.1016/j.optcom.2025.132327

Chen, Y., Deng, H., Sha, X., Chen, W., Wang, R., Chen, Y.-H., Wu, D., Chu, J., Kivshar, Y.S., Xiao, S., Qiu, C.-W.: Observation of intrinsic chiral bound states in the continuum. Nature. 613, 474–478 (2023). https://doi.org/10.1038/s41586-022-05467-6

Chen, Z., Huang, J., Tan, Q., Xiao, G., Sun, T., Zhang, F., Idris, A.S., Zou, Q., Li, H., Lu, G.: High-Sensitivity Optical Sensor Driven by the High-Q Quasi-Bound States in the Continuum of an Asymmetric

Bow-Tie Metasurface. Photonics. 13, 77 (2026). https://doi.org/10.3390/photonics13010077
Cheng, Y., Chen, J., Li, J., Liu, Z., Liu, W., Liu, G.: Ultra-High Q-Factors Dynamical Modulation in a Si-GSST Metasurface Induced by Quasi-BICs. IEEE Photonics Technology Letters. 36, 171–174 (2024). https://doi.org/10.1109/LPT.2023.3344484
Crotti, G., Akturk, M., Schirato, A., Vinel, V., Trifonov, A.A., Buchvarov, I.C., Neshev, D.N., Proietti Zaccaria, R., Laporta, P., Lemaître, A., Leo, G., Cerullo, G., Maiuri, M., Della Valle, G.: Giant ultrafast dichroism and birefringence with active nonlocal metasurfaces. Light Sci. Appl. 13, (2024). https://doi.org/10.1038/s41377-024-01545-8
Cui, T., Bai, B., Sun, H.-B.: Tunable Metasurfaces Based on Active Materials. Adv. Funct. Mater. 29, 1806692 (2019). https://doi.org/https://doi.org/10.1002/adfm.201806692
Ding, C., Rui, G., Gu, B., Zhan, Q., Cui, Y.: Phase-change metasurface with tunable and switchable circular dichroism. Opt. Lett. 46, 2525–2528 (2021). https://doi.org/10.1364/OL.423748
Guan, X., Xie, S., Zhuo, J., Sun, S.: Tunable circular dichroism supported by quasi-bound states in the continuum of a stretchable metasurface. Physica B Condens. Matter. 699, 416867 (2025). https://doi.org/https://doi.org/10.1016/j.physb.2024.416867
He, B., Liu, J., Cheng, Y., Chen, F., Luo, H., Li, X.: Broadband and thermally switchable reflective metasurface based on Z-shape InSb for terahertz vortex beam generation. Physica E Low. Dimens. Syst. Nanostruct. 144, 115373 (2022). https://doi.org/https://doi.org/10.1016/j.physe.2022.115373
He, Y., Guo, G., Feng, T., Xu, Y., Miroshnichenko, A.E.: Toroidal dipole bound states in the continuum. Phys. Rev. B. 98, (2018). https://doi.org/10.1103/PhysRevB.98.161112
Hsu, C.W., Zhen, B., Stone, A.D., Joannopoulos, J.D., Soljačić, M.: Bound states in the continuum. Nat. Rev. Mater. 1, 16048 (2016). https://doi.org/10.1038/natrevmats.2016.48
Hu, H., Lu, W., Antonov, A., Berté, R., Maier, S.A., Tittl, A.: Environmental permittivity-asymmetric BIC metasurfaces with electrical reconfigurability. Nature Communications . 15, (2024). https://doi.org/10.1038/s41467-024-51340-7
Hu, J., Chen, Y., Zhang, W., Tang, Z., Lan, X., Deng, Q., Cui, H., Li, L., Huang, Y.: Single-Layered Phase-Change Metasurfaces Achieving Polarization- and Crystallinity-Dependent Wavefront Manipulation. Photonics. 10, (2023). https://doi.org/10.3390/photonics10030344
Hu, L., Wang, B., Guo, Y., Du, S., Chen, J., Li, J., Gu, C., Wang, L.: Quasi-BIC Enhanced Broadband Terahertz Generation in All-Dielectric Metasurface. Adv. Opt. Mater. 10, (2022). https://doi.org/10.1002/adom.202200193
Icenogle, H.W., Platt, B.C., Wolfe, W.L.: Refractive indexes and temperature coefficients of germanium and silicon. Appl. Opt. 15, 2348–2351 (1976). https://doi.org/10.1364/AO.15.002348
Jia, Y., Zhang, X., Chen, J., Meng, H., Wu, H.: 3D intrinsic chiral BIC metasurface enabling strong linear and nonlinear CD with efficient THG. Phys. Scr. 100, 105515 (2025). https://doi.org/10.1088/1402-4896/ae0dc5
Jiang, C., He, L., Xuan, Q., Liao, Y., Dai, J.-G., Lei, D.: Phase-change VO2-based thermochromic smart windows. Light Sci. Appl. 13, 255 (2024). https://doi.org/10.1038/s41377-024-01560-9
Jiang, H., Peng, K., Cui, Y., Xie, Z., Zhang, H., Jiang, Y., Zhao, W., Yuan, X.: Giant and reversible circular dichroism based on phase change materials for near-field image display. Journal of Optics. 25, 065101 (2023)(a). https://doi.org/10.1088/2040-8986/acba2e
Jiang, X., Ji, Y.-Y., Fan, F., Jiang, S.-L., Tan, Z.-Y., Zhao, H., Cheng, J.-R., Chang, S.: Arbitrary terahertz chirality construction and flexible manipulation enabled by anisotropic liquid crystal coupled chiral metasurfaces. Photonics Res. (2023)(b). https://doi.org/10.1364/prj.501047

Kang, M., Liu, T., Chan, C.T., Xiao, M.: Applications of bound states in the continuum in photonics. Nature Reviews Physics. 5, 659–678 (2023). https://doi.org/10.1038/s42254-023-00642-8

Kang, M., Mao, L., Zhang, S., Xiao, M., Xu, H., Chan, C.T.: Merging bound states in the continuum by harnessing higher-order topological charges. Light Sci. Appl. 11, (2022). https://doi.org/10.1038/s41377-022-00923-4

Kim, K.-H., Cho, M.-C.: Tunable multiband circular dichroism and asymmetric transmission enabled by chiral quasi-BICs in dielectric metasurfaces covered with graphene. Opt. Mater. (Amst). 148, 114798 (2024). https://doi.org/https://doi.org/10.1016/j.optmat.2023.114798

Koshelev, K., Bogdanov, A., Kivshar, Y.: Meta-optics and bound states in the continuum. Sci. Bull. (Beijing). 64, 836–842 (2019). https://doi.org/https://doi.org/10.1016/j.scib.2018.12.003

Lai, F., Fan, Y., Sha, X., Deng, H., Jiang, X., Xiao, S., Huang, C., Song, Q.: Ultrafast polarization modulation with high-purity chiral quasi-BIC metasurfaces. Chinese Optics Letters. 23, 053605 (2025). https://doi.org/10.3788/col202523.053605

Lee, S., Seo, D., Park, S.H., Izquierdo, N., Lee, E.H., Younas, R., Zhou, G., Palei, M., Hoffman, A.J., Jang, M.S., Hinkle, C.L., Koester, S.J., Low, T.: Achieving near-perfect light absorption in atomically thin transition metal dichalcogenides through band nesting. Nat. Commun. 14, (2023). https://doi.org/10.1038/s41467-023-39450-0

Li, X., Han, Q., Li, X., Li, R., Wang, A., Liang, S., Sang, Y., Li, J., Tian, Y., Yang, Y., Li, Q., Bai, S., Li, J.: Chiroptical switching and strong circularly polarized luminescence in peptide supramolecular assemblies. Nature Communications . 16, (2025). https://doi.org/10.1038/s41467-025-61007-6

Liu, W., Wang, B., Zhang, Y., Wang, J., Zhao, M., Guan, F., Liu, X., Shi, L., Zi, J.: Circularly Polarized States Spawning from Bound States in the Continuum. Phys. Rev. Lett. 123, 116104 (2019). https://doi.org/10.1103/PhysRevLett.123.116104

Ma, T., Sang, W., Tian, J., Ma, L., Ma, L., Li, J.: Active control of circular dichroism in a graphene–metal hybridized metamaterial driven by symmetry-protected bound states in the continuum. Physical Chemistry Chemical Physics. 25, 29664–29671 (2023). https://doi.org/10.1039/d3cp03288d

Mahmud, A., Siddique, M.A.I., Jyoti, O.: Analyzing and Optimizing the Geometric Design of VO2 Based Metamaterial Unit Cells for Enhanced THz Absorption Bandwidth. In: 2024 6th International Conference on Electrical Engineering and Information & Communication Technology (ICEEICT). pp. 836–840 (2024)

Ouyang, S., Sang, T., Jing, Z., Lu, J.: Steering high-Q intrinsic chiral quasi-bound states in the continuum via engineered 2.5D phase-change metasurfaces. Opt. Lett. 49, 5703–5706 (2024). https://doi.org/10.1364/OL.534860

Overvig, A., Yu, N., Alù, A.: Chiral Quasi-Bound States in the Continuum. Phys. Rev. Lett. 126, 73001 (2021). https://doi.org/10.1103/PhysRevLett.126.073001

P, A., Chauhan, Y.S., Verma, A.: High infrared reflectance modulation in VO2 films synthesized on glass and ITO coated glass substrates using atmospheric oxidation of vanadium. Opt. Mater. (Amst). 110, 110438 (2020). https://doi.org/https://doi.org/10.1016/j.optmat.2020.110438

Pitilakis, A., Seckel, M., Tasolamprou, A.C., Liu, F., Deltsidis, A., Manessis, D., Ostmann, A., Kantartzis, N. V, Liaskos, C., Soukoulis, C.M., Tretyakov, S.A., Kafesaki, M., Tsilipakos, O.: Multifunctional Metasurface Architecture for Amplitude, Polarization and Wave-Front Control. Phys. Rev. Appl. 17, 64060 (2022). https://doi.org/10.1103/PhysRevApplied.17.064060

Sharma, S., Karabchevsky, A., Varshney, S.K.: Accidental BICs and Chiroptical Response of Hollow Channels in Silicon Nanodisk Resonator-Based Metasurfaces for Chiral Sensing. ACS Applied Optical

Materials. 3, 364–374 (2025). https://doi.org/10.1021/acsaom.4c00489
Shi, Z., He, J., Wu, Q., Shao, H., Dong, J.: Tunable circular dichroism in all-dielectric metasurface with efficient wavefront manipulation. Results Phys. 55, 107153 (2023). https://doi.org/https://doi.org/10.1016/j.rinp.2023.107153
Svoboda, R., Bezdička, P., Gutwirth, J., Málek, J.: Crystallization processes in Ge2Sb2Se4Te glass. Mater. Res. Bull. 61, 207–214 (2015). https://doi.org/https://doi.org/10.1016/j.materresbull.2014.10.032
Tang, Z., Li, C., Pan, R., Wang, B., Liu, Y., Wang, Q., Tan, J., Xiang, Y., Yang, H., Li, J.: Ge2Sb2Se4Te-Based Optical Switch with Ultra-High Contrast Ratio by Multilayer Fabry–Perot Cavity. Advanced Science. 12, (2025). https://doi.org/10.1002/advs.202412499
Wang, C., Wang, R., Cheng, X., Hu, X., Wang, C.: Passively Broadband Tunable Dual Circular Dichroism via Bound States in the Continuum in Topological Chiral Metasurface. ACS Nano. 18, 18922–18932 (2024). https://doi.org/10.1021/acsnano.4c01697
Wang, M., Huang, Z., Salut, R., Suarez, M., Lu, H., Martin, N., Grosjean, T.: Plasmonic Helical Nanoantenna As a Converter between Longitudinal Fields and Circularly Polarized Waves. Nano Lett. 21, (2021). https://doi.org/10.1021/acs.nanolett.0c04948
Wang, Y., Liu, G., Peng, Y., Huang, Z., Song, X., Ren, K., Bai, J., Chen, R., Bai, Y., Fu, T., Dong, J.: Active control and sensing application of ultra-narrowband circular dichroism in the multilayer complementary chiral metasurface. Opt. Commun. 620, 133633 (2026). https://doi.org/https://doi.org/10.1016/j.optcom.2026.133633
Wu, Q., Shi, Z., He, J., Dong, J.: An all-dielectric chiral metasurface with circular dichroism and asymmetric transmission characteristics. Optoelectron. Lett. 20, 537–542 (2024). https://doi.org/10.1007/s11801-024-3231-1
Xia, H., You, T., Luo, D., Xiong, D.: Quasi-BIC enabled critical coupling for high-Q near-perfect infrared absorption. Photonics Nanostruct. 71, (2026). https://doi.org/10.1016/j.photonics.2026.101583
Xie, S., Sun, S., Shen, W., Yang, J., Guan, X., Chen, J., Zeng, Z., Sun, M.: Bilayer Metasurface With High-Q Terahertz Chiroptical Response Empowered by Intrinsic Quasi-Multi-Bound States in the Continuum. Journal of Lightwave Technology. 42, 7765–7775 (2024)
Xiong, B., Liu, Y., Xu, Y., Deng, L., Chen, C.-W., Wang, J.-N., Peng, R., Lai, Y., Liu, Y., Wang, M.: Breaking the limitation of polarization multiplexing in optical metasurfaces with engineered noise. Science (1979). 379, 294–299 (2023). https://doi.org/10.1126/science.ade5140
Xu, C., Liu, J., Song, G.: Giant Circular Dichroism in Chiral Broad Flat-Band Quasi-BIC Metasurface. Nanophotonics. 15, (2026). https://doi.org/10.1002/nap2.70106
Xu, S.-T., Fan, J., Xue, Z., Sun, T., Li, G., Li, J., Lu, D., Cong, L.: Active control of terahertz quasi-BIC and asymmetric transmission in a liquid-crystal-integrated metasurface. Photonics Res. 12, 2207 (2024). https://doi.org/10.1364/prj.531952
Yang, H., Sun, H., Yang, Y., He, Q., Li, J., Xiao, G.: High-Q terahertz chirality enhancement using elliptical hole metasurface. Opt. Commun. 575, 131268 (2025). https://doi.org/https://doi.org/10.1016/j.optcom.2024.131268
Ye, Z., Fan, Y., Sun, K., Qiu, W., Wang, H., Shi, H., Zeng, Y., Zhang, F.: Dual quasi-bound state enhanced second harmonic generation in lithium niobate metasurfaces. Opt. Quantum Electron. 56, (2024). https://doi.org/10.1007/s11082-024-07902-6
Zeng, D., Wu, Z., Liu, G., Yu, M., Liu, X., Chen, J., Tang, C., Du, W., Liu, Z.: Ultra-slow-light and dynamically quantitative optical storage modulation via quasi-BICs. Opt. Lett. 49, 3030–3033 (2024). https://doi.org/10.1364/OL.524580

Zeng, X., Rosenmann, D., Czaplewski, D.A., Gao, J., Yang, X.: Chiral metasurfaces of wavy rectangle resonators with tunable circular dichroism. Optik (Stuttg). 286, 171024 (2023). https://doi.org/https://doi.org/10.1016/j.ijleo.2023.171024

Zeng, Z., Xie, S., Sun, M., Chen, J., Sun, S., Guan, X.: Tunable chiral quasi-bound states in the continuum in terahertz metasurfaces. Physica B Condens. Matter. 713, 417350 (2025). https://doi.org/https://doi.org/10.1016/j.physb.2025.417350

Zhang, D., Liu, T., Lei, L., Deng, W., Wang, T., Liao, Q., Liu, W., Xiao, S., Yu, T.: Tailoring intrinsic chirality in a two-dimensional planar waveguide grating via quasibound states in the continuum. Phys. Rev. B. 109, (2024). https://doi.org/10.1103/PhysRevB.109.205403

Zhang, Y., Chou, J.B., Li, J., Li, H., Du, Q., Yadav, A., Zhou, S., Shalaginov, M.Y., Fang, Z., Zhong, H., Roberts, C., Robinson, P., Bohlin, B., Ríos, C., Lin, H., Kang, M., Gu, T., Warner, J., Liberman, V., Richardson, K., Hu, J.: Broadband transparent optical phase change materials for high-performance nonvolatile photonics. Nature Communications . 10, (2019). https://doi.org/10.1038/s41467-019-12196-4

Zhang, Y., Fowler, C., Liang, J., Azhar, B., Shalaginov, M.Y., Deckoff-Jones, S., An, S., Chou, J.B., Roberts, C.M., Liberman, V., Kang, M., Ríos, C., Richardson, K.A., Rivero-Baleine, C., Gu, T., Zhang, H., Hu, J.: Electrically reconfigurable non-volatile metasurface using low-loss optical phase-change material. Nat. Nanotechnol. 16, 661–666 (2021). https://doi.org/10.1038/s41565-021-00881-9

Zhou, S., Liu, L., Chen, Z., Ansari, M.A., Chen, X., Chan, M.: Polarization-multiplexed metaholograms with erasable functionality. J. Phys. D Appl. Phys. 56, 155102 (2023). https://doi.org/10.1088/1361-6463/acbf61

Supplementary Files

This is a list of supplementary files associated with this preprint. Click to download.

- SupportingInformation.docx